

Pedestal Structure Without And With 3D Fields

J.D. Callen,*

Department of Engineering Physics, University of Wisconsin, Madison, WI 53706-1609 USA

Key words tokamak, pedestal, transport, paleoclassical, 3D field effects

Achieving high pedestal pressures in H(high)-mode plasmas confined in tokamaks is critical for obtaining fusion burning plasmas in ITER. Recent characterizations of quasi-equilibrium plasma parameter profiles in low collisionality H-mode pedestals in the DIII-D tokamak are briefly summarized. Critical plasma transport properties (large radial electron heat flow, density pinch) that establish the transport barrier structure of the pedestal profiles are identified. The paleoclassical transport model, which naturally includes a density pinch, is shown to provide the minimum electron heat and density transport in the pedestal. Microinstabilities can provide additional plasma transport within and especially at the top of pedestals. Macroscopic peeling-ballooning (P-B) instabilities cause periodic edge localized modes (ELMs) that limit the temporal and spatial growth of the pedestal initially and between ELMs. Externally imposed 3D resonant magnetic perturbations (RMPs) in the pedestal have been used to stabilize P-B modes and suppress ELMs. A magnetic flutter model of plasma transport induced by the 3D RMPs has been developed for low collisionality DIII-D pedestals. Comparisons of it with data on ELM suppression by RMPs indicate it can provide a “diffusivity hill” at the pedestal top that can impede pedestal growth and thereby stabilize P-B modes and suppress ELMs. Finally, transport equations for plasma density, electron and ion pressures and, most importantly, the plasma toroidal rotation frequency (and hence, via radial force balance, the radial electric field) in the presence of plasma transport due to collisional, paleoclassical, microturbulence-induced and 3D field effects are presented.

Copyright line will be provided by the publisher

1 Motivation and introduction

Significant fusion power production in ITER [1] will require H(high)-confinement mode plasmas with large pedestal pressures. The pedestal pressure height and width in H-mode tokamak plasmas are limited by ideal magnetohydrodynamic (MHD) peeling-ballooning (P-B) instabilities [2]. These instabilities cause roughly periodic edge-localized-modes (ELMs) that abruptly relax the large edge plasma gradients and deposit undesirable bursts of plasma heat and particles on divertor plates. Pedestals evolve in various stages after an ELM [3]. Within typically 10 ms after an ELM crash the pedestal re-establishes itself. But then it continues to grow slowly (for 10s of ms or longer) until a P-B instability precipitates an ELM. Externally imposed three-dimensional (3D) resonant magnetic perturbations (RMPs) have been used in DIII-D [4] to limit this progression and mitigate [5, 6, 7] or suppress [8] ELMs in tokamaks. The present challenge for edge plasma modeling is to develop and experimentally validate predictive transport models for the profiles and evolution of the pedestal density, temperature, flow and radial electric field profiles with and without 3D fields. This paper mainly reviews recent research results [9]–[16] on key paleoclassical and 3D transport processes involved in determining the structure of plasma profiles in low collisionality H-mode pedestals without [9] and with [8] RMPs in ITER-similar-shape DIII-D plasmas. The emphasis is on a validation process comparing theoretical models to relevant experimental data.

This paper is organized as follows. The next section provides a characterization of key plasma transport processes involved in a typical low collisionality H-mode pedestal in DIII-D. This is followed by a summary of the results of validation studies of paleoclassical transport model predictions in the pedestal region. Section 4 then discusses the additional non-ambipolar electron transport induced by externally imposed 3D fields in the pedestal region. There, the emphasis is on the change in the radial electric field the RMPs induce and resultant changes in the net ambipolar density and electron heat transport at the top of the pedestal. This is followed by a section that presents comprehensive transport equations for modeling the structure and evolution of plasma profiles in the pedestal region. The final section summarizes the primary conclusions of this paper and identifies other physical models needed for development of a predictive capability of pedestals with and without 3D fields.

* callen@engr.wisc.edu, <http://homepages.cae.wisc.edu/~callen>

2 Plasma properties and transport in a low collisionality DIII-D pedestal

The characteristics, key parameters and plasma transport properties of the pedestal in a DIII-D discharge with an ITER-relevant low collisionality were presented in Ref. [9]. This paper resulted from a benchmarking exercise that used 5 transport codes (ONETWO, ASTRA, GTEDGE, SOLPS, UEDGE) in interpretive analysis modes to study the quasi-equilibrium transport state (last 80-99 % of 33.5 ms average period between ELMs) of the pedestal in DIII-D discharge #98889. Key plasma profiles of this discharge’s pedestal, which are typical of most low density and collisionality pedestals with and without externally applied RMPs in DIII-D are shown in Fig. 1.

The radial coordinate in Fig. 1 is the normalized radius $\rho_N \equiv \rho/a$ ($a \simeq 0.77$ m) in which $\rho \equiv \sqrt{\psi_t/\pi B_{t0}}$ is the toroidal-flux-based minor radius (m). Identified pedestal regions here are:

I, core, $0.85 < \rho_N < 0.96$,

II, top half, $0.96 < \rho_N < 0.98$ and

III, bottom half, $0.98 < \rho_N < 1.0$.

Key pedestal profile features are: n_e is “aligned” with the T_e profile, $dT_e/d\rho \simeq \text{constant}$ in the pedestal steep gradient region (**II and III**), and T_i has the smallest gradient. The “transport barrier” minimum effective diffusivities at the pedestal mid-point ($\rho_N \simeq 0.98$) are quite small: 0.3 (electron heat), 0.15 (ion heat) and 0.035 (density) $\text{m}^2 \text{s}^{-1}$. The very small effective density diffusivity can be explained [9] as being the result of an inward pinch flow nearly balancing the diffusive outward density flux. The inward pinch velocity and density diffusivity were determined using an innovative interpretive analysis [17] of pedestal plasma flows. The paleoclassical transport model [18] provides a plausible explanation of them. The particle source from edge fueling plays a minor role compared to density pinch effects in determining the edge density profile in this pedestal [9].

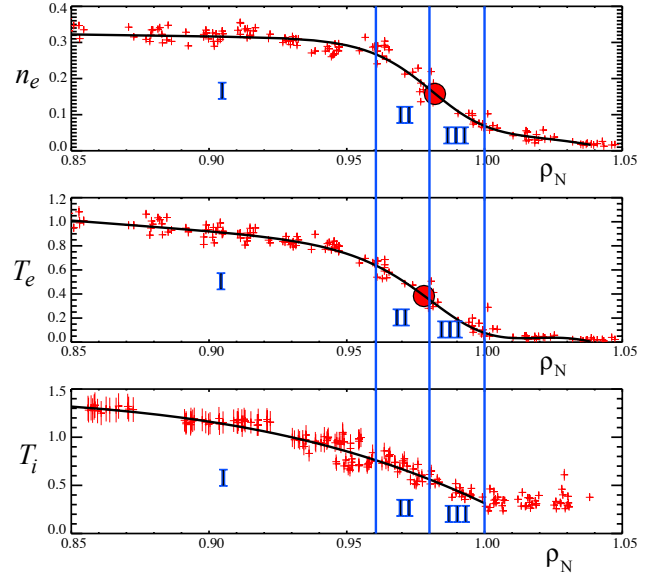


Fig. 1 Profiles of electron density (10^{20} m^{-3}) and temperature (keV), and ion temperature (keV) in the edge of DIII-D discharge #98889 [9]. Lines show tanh profile and spline fits; red dots are fit symmetry points (pedestal mid-points). Adapted from Ref. [10].

3 Pedestal structure modeling with the paleoclassical transport model

The electron temperature is low in H-mode pedestals (e.g., $T_e \sim 100 - 700$ eV in **III and II** in Fig. 1). It has been hypothesized [19] that paleoclassical transport [18] dominates over gyro-Bohm-level transport where $T_e \lesssim B(\text{T})^{2/3} a(\text{m})$ keV. The paleoclassical transport model has been validated to a fair degree for such low T_e values [19], which are satisfied by the DIII-D pedestal profiles shown in Fig. 1. Thus, a pedestal structure model [10] based on paleoclassical transport has been developed recently and validation studies undertaken [10]–[12].

The initial paleoclassical model [18] was based on a key hypothesis that charged particles diffuse radially along with thin annuli of poloidal magnetic flux in resistive, current-carrying toroidal plasmas. That is, they diffuse radially with the resistivity-induced magnetic field diffusivity $D_\eta \equiv \eta/\mu_0$. This hypothesis was later shown [20] to result from transforming the drift-kinetic equation from laboratory to poloidal flux coordinates, upon which Grad-Shafranov equilibria, neoclassical transport theory, and gyrokinetic-based anomalous transport analyses are based. A Comment [21] on [20] asserted the effects “appear to lack a systematic basis.” The Response [22] provided a systematic multiple-time-scale analysis of electron guiding center motion that produces these effects.

The fundamental parameter of the paleoclassical transport model is the diffusivity coefficient ($\text{m}^2 \text{s}^{-1}$) for diffusion of the poloidal magnetic flux [18]–[20], which is caused by the parallel neoclassical resistivity $\eta_{\parallel}^{\text{nc}}$

$$D_\eta \equiv \frac{\eta_{\parallel}^{\text{nc}}}{\mu_0} = \frac{\eta_0}{\mu_0} \frac{\eta_{\parallel}^{\text{nc}}}{\eta_0}, \quad \text{magnetic field diffusivity,} \quad \frac{\eta_0}{\mu_0} \equiv \frac{m_e \nu_e}{\mu_0 n_e e^2} \simeq \frac{1400 Z}{[T_e(\text{eV})]^{3/2}} \left(\frac{\ln \Lambda}{17} \right). \quad (1)$$

Here and below, $Z \rightarrow Z_{\text{eff}} \equiv \sum_i n_i Z_i^2 / n_e$ is the effective ion charge and $\ln \Lambda$ is the Coulomb logarithm.

A useful and physically illustrative approximate formula for the ratio of neoclassical resistivity to η_0 is [18] $\eta_{\parallel}^{\text{nc}} / \eta_0 \simeq \eta_{\parallel}^{\text{Sp}} / \eta_0 + \mu_e / \nu_e$. The Spitzer ($\eta_{\parallel}^{\text{Sp}} / \eta_0$) and viscous damping (μ_e / ν_e) parts of $\eta_{\parallel}^{\text{nc}}$ are [10, 23] $\eta_{\parallel}^{\text{Sp}} / \eta_0 \simeq (\sqrt{2} + Z) / (\sqrt{2} + 13 Z / 4)$, $\mu_e / \nu_e \simeq (f_t / f_c) (1 + 0.533 / Z) / \{ [1 + \sqrt{\nu_{*e}} + 1.65 (1 + 0.533 / Z) \nu_{*e}] [1 + \nu_e / \omega_{te}] \}$. Here, μ_e is the electron viscous damping rate for collisions of flow-carrying untrapped electrons with trapped electrons and $\omega_{te} \equiv v_{Te} / R_0 q$ is the electron transit frequency for the electron thermal speed $v_{Te} \equiv \sqrt{2 T_e / m_e}$. Also, f_c is the flow-weighted fraction of circulating particles [24] $f_c \equiv (3/4) \langle B^2 \rangle \int_0^{1/B_{\text{max}}} \lambda d\lambda / \langle \sqrt{1 - \lambda B(\theta)} \rangle$ with Padé approximate [25] $f_c \simeq (1 - \epsilon^2)^{-1/2} (1 - \epsilon)^2 / (1 + 1.46 \epsilon^{1/2} + 0.2 \epsilon)$, in which $\langle \dots \rangle$ indicates the flux surface average and $\epsilon \equiv (B_{\text{max}} - B_{\text{min}}) / (B_{\text{max}} + B_{\text{min}}) \simeq r_M / R_0$ is the local magnetic inverse aspect ratio. For $\epsilon \ll 1$, $f_c \simeq 1 - 1.46 \epsilon^{1/2}$. The fraction of trapped particles is $f_t \equiv 1 - f_c$. For the DIII-D pedestal [9] in Fig. 1, $\epsilon \simeq 0.35$ and $f_t / f_c \simeq 0.77 / 0.23 \simeq 3.3 \gg 1$. For NSTX [11] $f_t / f_c \simeq 0.93 / 0.07 \sim 13$ is very large.

The neoclassical electron collisionality parameter for the large f_t / f_c values in H-mode pedestals is [24, 26, 27]

$$\nu_{*e} \equiv \frac{(f_t / f_c) \nu_e \langle B^2 \rangle / R_0 q}{2.92 v_{Te} \langle (\hat{\mathbf{b}} \cdot \nabla B)^2 \rangle} \simeq \frac{f_t / f_c}{1.46 \epsilon^2} \frac{\nu_e}{\omega_{te}} = \frac{f_t / f_c}{1.46 \epsilon^2} \frac{R_0 q}{\lambda_e} \stackrel{\epsilon \ll 1}{\simeq} \frac{\nu_e}{\epsilon^{3/2} \omega_{te}}. \quad (2)$$

Here, $\langle (\hat{\mathbf{b}} \cdot \nabla B)^2 \rangle / \langle B^2 \rangle \simeq \epsilon^2 / 2 R_0^2 q^2$. The ν_e and hence $\nu_e / \epsilon^{3/2} \omega_{te}$ are $\sqrt{2}$ smaller than in Refs. [28] and [29]. The electron Coulomb collision length is $\lambda_e \equiv v_{Te} / \nu_e \simeq 1.2 \times 10^{16} [T_e (\text{eV})]^2 (17 / \ln \Lambda) / [Z n_e (\text{m}^{-3})] \text{ m}$.

Because the fraction of trapped particles f_t is large in most tokamak H-mode pedestals, the relevant electron collisionality parameter ν_{*e} is larger than the usual [28] $\nu_e / \epsilon^{3/2} \omega_{te}$ formula by a factor of $(f_t / f_c) / (1.46 \epsilon^{1/2})$. At the mid-point of the $1/\epsilon \sim 2.8$ DIII-D pedestal in Fig. 1 $\nu_{*e}(\rho_{\text{mid}}) \simeq 3.9$ is a factor of about 4 larger than the usual $\epsilon \ll 1$ result of 1.0 there [9]. Thus, because of their low aspect ratio, pedestal plasmas are typically not in the low collisionality ($\nu_{*e} \ll 1$) ‘‘banana’’ regime; rather, they are usually in the ‘‘plateau’’ or even Pfirsch-Schlüter ($\nu_e > \omega_{te}$) regimes [28, 24]. This is especially true for very low aspect ratio tokamaks such as NSTX [11], Pegasus [30] and MAST [7]. The normalized electron viscosity coefficient μ_e / ν_e increases significantly in H-mode pedestals from the separatrix inward; e.g., for the DIII-D pedestal in Fig. 1 it is negligible at the separatrix but increases the resistivity by a factor of 2.4 over the Spitzer value at the pedestal top ($\rho_N \simeq 0.96$).

In a transport quasi-equilibrium where $\partial / \partial t$ terms are negligible the flux-surface-average (FSA) density and electron energy balance equations are $\langle \nabla \cdot \mathbf{\Gamma} \rangle = \langle S_n \rangle$ and $\langle \nabla \cdot \mathbf{q}_e^{\text{pc}} \rangle + \langle \nabla \cdot [\mathbf{q}_e^{\text{other}} + (5/2) T_e \mathbf{\Gamma}] \rangle = Q_e^{\text{net}}$. The FSAs are simplified using $\langle \nabla \cdot \mathbf{A} \rangle = (1/V') (\partial / \partial \rho) (V' A)$ in which $A \equiv \langle \mathbf{A} \cdot \nabla \rho \rangle$ and $V' \equiv dV(\rho) / d\rho$ where $V(\rho)$ is the volume of the ρ flux surface. The FSA paleoclassical transport flux contributions are [18, 10]

$$\Gamma^{\text{pc}} = -\frac{1}{V'} \frac{\partial}{\partial \rho} (V' \bar{D}_\eta n) = -\bar{D}_\eta \frac{dn}{d\rho} + n V_{\text{pinch}}, \quad \langle \nabla \cdot \mathbf{q}_e^{\text{pc}} \rangle = -\frac{M+1}{V'} \frac{d^2}{d\rho^2} \left(V' \bar{D}_\eta \frac{3}{2} n_e T_e \right). \quad (3)$$

Here, $\Gamma^{\text{pc}} \equiv \langle \Gamma^{\text{pc}} \cdot \nabla \rho \rangle$ and $\bar{D}_\eta \equiv D_\eta \langle |\nabla \rho|^2 / R^2 \rangle / \langle R^{-2} \rangle$ is the geometrically-averaged magnetic field diffusivity which is about $1.6 D_\eta$ for the pedestal in Fig. 1. As indicated in (3), paleoclassical transport is non-standard. First, the (ambipolar [18]) density flux naturally includes an inward pinch flow $V_{\text{pinch}} \equiv -(1/V') (d/d\rho) (V' \bar{D}_\eta n)$. Second, the paleoclassical contribution to the electron energy balance is not in the standard form $\langle \nabla \cdot \mathbf{q} \rangle = (1/V') (\partial / \partial \rho) (V' \langle \mathbf{q} \cdot \nabla \rho \rangle)$; rather, it has a second derivative multiplied by a factor [18] $M \simeq \lambda_e / \pi R_0 q$ in the pedestal region, which ranges from 0 at the separatrix to about 3 at the pedestal top for the pedestal in Fig. 1.

Pedestal plasma transport is dominated by the heat from the core flowing through it and edge fueling via neutral recycling from outside the separatrix. The paleoclassical density equation can be integrated from the separatrix ($\rho = a$) inward to yield $-(d/d\rho) (V' \bar{D}_\eta n) = \dot{N}(\rho) \equiv \dot{N}(a) - \int_\rho^a d\hat{\rho} V'(\hat{\rho}) \langle S_n(\hat{\rho}) \rangle$ in which $\dot{N}(\rho)$ is the number of particles flowing across the ρ flux surface per second. Integrating this result for electrons from a reference radius ρ_{ref} to ρ yields [10] (for regions II and III in Fig. 1)

$$n_e(\rho) \bar{D}_\eta(\rho) V'(\rho) = n_e(\rho_{\text{ref}}) \bar{D}_\eta(\rho_{\text{ref}}) V'(\rho_{\text{ref}}) + \int_\rho^{\rho_{\text{ref}}} d\hat{\rho} \dot{N}(\hat{\rho}) \implies \boxed{n_e^{\text{pc}}(\rho) \simeq \frac{\text{constant}_n}{\bar{D}_\eta(\rho)}}. \quad (4)$$

Since $V'(\rho) \simeq \text{constant}$ in the pedestal and the density source $\dot{N}(\rho)$ is typically small compared to the characteristic rate of paleoclassical density flow $-(d/d\rho) (V' \bar{D}_\eta n)$ there ($\lesssim 10\%$ for the DIII-D pedestal in Fig. 1

[10]), this yields the boxed prediction for $n_e(\rho)$ in which $\text{constant}_n \equiv n_e(\rho_{\text{ref}}) \bar{D}_\eta(\rho_{\text{ref}})$. Thus, the pedestal n_e profile is predicted to be proportional to $1/\bar{D}_\eta \propto T_e^{3/2}/[Z_{\text{eff}}(\eta_{\parallel}^{\text{Sp}}/\eta_0 + \mu_e/\nu_e)]$, which is $\propto T_e^{3/3}$ to lowest order but reduced by dependences of Z_{eff} and μ_e/ν_e on T_e . This predicted density profile produces a small net radial paleoclassical density flux in (3) by nearly balancing the paleoclassical outward diffusive density flux with a large inward paleoclassical pinch flux, in agreement with the results obtained in [9] for the DIII-D pedestal in Fig. 1. This result also implies that the n_e profile will be aligned with the T_e profile in the pedestal and will “saturate” along with T_e at the pedestal top, where microinstability-induced anomalous transport often becomes dominant.

A similar radial integration of the electron energy balance assuming paleoclassical electron heat transport dominates yields [10] $-V'\bar{D}_\eta n_e (3/2)(dT_e/d\rho) + (3/2)\dot{N}_e T_e = P_e$ in which $P_e(\rho)$ is the effective conductive heat flow (W) through the ρ flux surface. Neglecting again the typically negligible \dot{N} contribution (here $\lesssim 3\%$ for the DIII-D pedestal in Fig. 1 [9]) yields the predictions [10, 23] (for regions **II** and **III** in Fig. 1):

$$-\frac{dT_e^{\text{pc}}}{d\rho} = \frac{P_e}{(3/2)[V'\bar{D}_\eta n_e]} \simeq \text{constant}_T \implies \boxed{\chi_{e\text{eff}}^{\text{pc}} \equiv \frac{P_e/(V'\langle|\nabla\rho|^2\rangle)}{-n_e dT_e^{\text{pc}}/d\rho} = \frac{3/2}{\langle|\nabla\rho|^2}\bar{D}_\eta \simeq D_\eta.} \quad (5)$$

This result predicts the gradient of T_e will become large enough for the large electron heat flux from the core to flow through the pedestal at the rate determined by paleoclassical electron heat transport with an effective thermal diffusivity $\chi_{e\text{eff}}^{\text{pc}}$. As indicated in (5), since for core heated H-mode plasmas P_e is nearly constant in the pedestal and from (4) the quantity $[V'\bar{D}_\eta n_e]$ is also spatially constant there, the paleoclassical prediction is that the T_e gradient is spatially constant in the pedestal, as is roughly the case in Fig. 1. The boxed equation in (5) indicates the effective electron thermal diffusivity $\chi_{e\text{eff}}^{\text{pc}}$ is D_η times some geometric coefficients ($\chi_{e\text{eff}}^{\text{pc}} \simeq 1.2D_\eta$ [10] for the DIII-D pedestal in Fig. 1). This $\chi_{e\text{eff}}^{\text{pc}}$ prediction in regions **II** and **III** is different from the usual local paleoclassical estimate [18] of $\chi_e^{\text{pc}} \simeq (3/2)(M+1)D_\eta$ because [10] there is little local electron heating there and the paleoclassical heat transport operator shown in (3) is non-standard. Paleoclassical predictions for $T_e^{\text{pc}}(\rho)$ in the core region **(I)** require taking account of this non-standard electron heat transport operator.

Since the density prediction in (4) is about a factor of about two high [12], additional density transport may be needed near the separatrix. Since experimental uncertainties in the $dT_e/d\rho$ comparisons include equality [12], the paleoclassical model provides the minimum electron heat transport in the steep gradient region (**II,III**); however, additional electron heat transport likely occurs there at high β_p and T_e (low D_η) [12] and in the core region **(I)**.

4 Magnetic flutter model of additional plasma transport induced by 3D fields

Reference [31] reviews all the toroidal torques and non-ambipolar ion transport small non-axisymmetric (3D) magnetic fields cause in tokamaks. The focus here is on externally applied resonant magnetic perturbations (RMPs) used to suppress ELMs in low collisionality pedestals in DIII-D plasmas [8]. The principal RMP-induced effects there are: density “pump-out” [8] (pedestal density reduction), flattening of the T_e and n_e profiles at the pedestal top [13] (regions **I** and **II** in Fig. 1), limited windows in q_{95} for ELM suppression, and a “transport wall” at the pedestal top that halts [32, 33] the usual pedestal growth up to the P-B instability boundary.

An initial hypothesis [5] for how RMPs suppress ELMs assumed multiple RMPs produce overlapping islands that cause magnetic stochasticity, which would induce additional transport, reduce the pressure gradient in the edge and stabilize P-B modes. However, extended MHD calculations usually predict [34]–[39] that extant, mostly diamagnetic-flow-driven edge plasma toroidal flows limit “penetration” of RMP fields and thereby cause RMP-induced radial perturbations to be small on most pedestal rational ($q = m/n$) magnetic flux surfaces. This toroidal “flow screening” inhibits but does not entirely eliminate magnetic reconnection, island formation and stochasticity. In this situation the magnetic field structure [37, 39] at the pedestal top is characterized by radially separated chains of magnetic islands with sinusoidal radial magnetic flutter of field lines between them [15].

A novel flutter model of the plasma transport induced by RMPs has been developed recently [13, 14, 15]. In it, the perturbed current $\delta J_{\parallel m/n} \equiv -e \int d^3v v_{\parallel} \delta f_{e m/n}$ along the axisymmetric equilibrium magnetic field \mathbf{B}_0 caused by a single Fourier radial magnetic perturbation $\delta \hat{B}_{\rho m/n} e^{im\theta - in\zeta}$ induced by RMPs is calculated first. Since kinetic electron collisional effects on the untrapped electrons cause this to have a component in phase with the $\delta B_{\rho m/n}$ perturbation [13, 14], this produces a toroidal Maxwell stress torque and consequent FSA radial density flux $\Gamma^{\text{flutt}} = \langle \overline{\delta J_{\parallel m/n} \delta B_{\rho m/n}^*} \rangle / e\psi'_p$ in which the overline indicates an average over the axisymmetric

toroidal angle ζ and $\psi'_p \equiv d\psi_p/d\rho = RB_p$ is the radial derivative of the poloidal magnetic flux $2\pi\psi_p$. The physically relevant toroidal model [14] uses a Lorentz collision model, accounts for parallel flows only being carried by untrapped (circulating) particles, resolves a collisional boundary layer in velocity space, and includes near-separatrix toroidal geometry and finite inverse aspect ratio effects. The toroidal model [14] flutter-induced radial transport fluxes of electron density $\Gamma_e^{\text{flutt}} \equiv \langle \mathbf{\Gamma}_e^{\text{flutt}} \cdot \nabla \rho \rangle$ and heat $\Upsilon_e^{\text{flutt}} \equiv \langle \mathbf{q}_e \cdot \nabla \rho \rangle$ can be written as

$$\begin{bmatrix} \Gamma_e^{\text{flutt}} \\ \Upsilon_e^{\text{flutt}}/T_e \end{bmatrix} = -n_e \begin{bmatrix} D_e & D_T \\ \chi_n & \chi_e \end{bmatrix} \cdot \begin{bmatrix} d \ln \hat{p}_e / d\rho \\ d \ln T_e / d\rho \end{bmatrix}, \quad (6)$$

in which the relevant thermodynamic radial forces are proportional to

$$\frac{d \ln \hat{p}_e}{d\rho} = \frac{d \ln p_e}{d\rho} - \frac{e}{T_e} \frac{d\Phi_0}{d\rho} = \frac{d \ln p_e}{d\rho} + \frac{eE_\rho}{T_e}, \quad \text{and} \quad \frac{d \ln T_e}{d\rho} = \frac{1}{T_e} \frac{dT_e}{d\rho}. \quad (7)$$

The total magnetic-flutter-induced diffusivities are obtained by summing over all the m, n components:

$$\begin{bmatrix} D_e & D_T \\ \chi_n & \chi_e \end{bmatrix} = \sum_{mn} \begin{bmatrix} D_e^{m/n} & D_T^{m/n} \\ \chi_n^{m/n} & \chi_e^{m/n} \end{bmatrix} \equiv \frac{v_{Te}^2}{\nu_e} \frac{1}{2} \sum_{mn} \left(\frac{\langle \delta \hat{B}_{\rho m/n}^{\text{pl}} \rangle}{B_{t0}} \right)^2 \begin{bmatrix} K_{00} & K_{01} \\ K_{10} & K_{11} \end{bmatrix}. \quad (8)$$

Here, the pl superscript in $\langle \delta \hat{B}_{\rho m/n}^{\text{pl}} \rangle$ indicates the RMP-induced 3D fields are to be evaluated including plasma toroidal flow-screening effects and B_{t0} is the toroidal magnetic field strength at the magnetic axis. The K_{ij} matrix coefficients are Onsager-symmetric (i.e., $K_{01} = K_{10}$) that involve integrals over the electron energy distribution. They are highly peaked within a few mm around rational surfaces (in singular layers or thin islands) where the flutter diffusivities scale as $1/\nu_e$. However, the K_{ij} decrease with radius away from rational surfaces [13, 14, 15] and cause the flutter diffusivities to scale as $\sim \sqrt{\nu_e}$ [15] midway between rational surfaces. This decrease is partially compensated by the increase of the externally driven $\langle \delta \hat{B}_{\rho m/n}^{\text{pl}} \rangle$ [39, 16] away from rational surfaces.

Paloclassical predictions for profiles of the effective electron thermal diffusivity (5) and electron density (4) are compared with experimental data from DIII-D [10] and NSTX [11] in Figs. 2 and 3. Figure 2 shows n_e^{pc} and $\chi_{e,\text{eff}}^{\text{pc}}$ agree well with the DIII-D data in the pedestal steep gradient region (II and III). Figure 3 shows similar modeling results for plasmas in NSTX without and with lithium-coated plasma-facing components, which strongly modified the carbon density and Z_{eff} profiles in the pedestal. No anomalous electron heat transport is needed for the case with lithium in to $\Psi_N \simeq 0.8$. In the core (I) paleoclassical electron heat transport needs to be evaluated using the operator in (3); anomalous transport is also usually important there.

A statistical analysis [12] of the DIII-D pedestal database (158 conditions) found that at the pedestal midpoint $n_e^{\text{pc}}/n_e^{\text{exp}} \simeq 2.1 \pm 0.7$ with a correlation coefficient of 0.89 and $(dT_e^{\text{pc}}/d\rho)/(dT_e^{\text{exp}}/d\rho) \simeq 1.7 \pm 1.1$ with a correlation coefficient of 0.55.

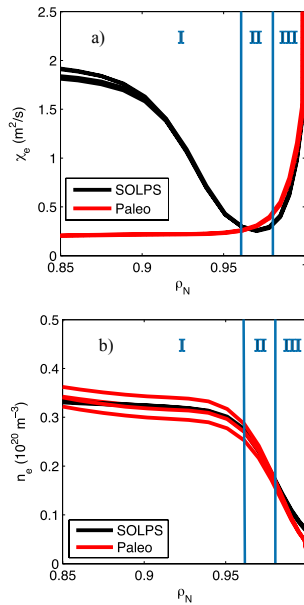


Fig. 2 Comparison of paleoclassical predictions (red/grey lines) and SOLPS interpretive modeling [11] (black lines) for 4 carbon (Z_{eff}) transport models for the DIII-D pedestal in Fig. 1. Adapted from Ref. [10].

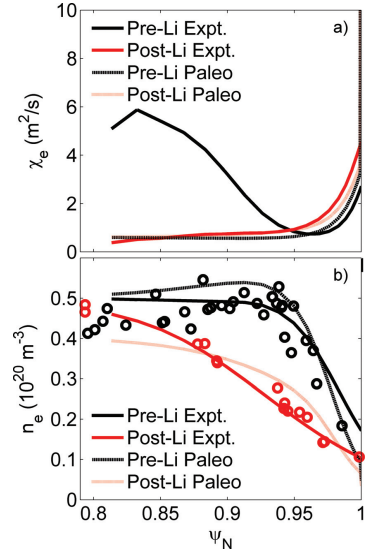


Fig. 3 Comparison of paleoclassical predictions (red) in (5) and (4) to SOLPS interpretive modeling [11] (in black) for NSTX edge without (Pre-Li) and with (Post-Li) lithium-coated plasma-facing components. The radial variable Ψ_N is the normalized poloidal magnetic flux. Copyright © 2011 American Institute of Physics.

Figure 4 compares flutter model predictions to experimental results [16]. In numerically evaluating (8) the RMP-induced perturbations $\langle \delta \hat{B}_{\rho m/n}^{pl} \rangle$ have been obtained using the M3D-C1 extended MHD code [38, 39]. Dotted vertical lines in Fig. 4 indicate radial locations of $q = m/n$ rational surfaces. After applying the ambipolar constraint [15] that $\Gamma_e^{\text{flutt}} = 0$, the effective $\chi_e^{\text{flutt}} = (4/13) \chi_e$. Since, as in (5) $-dT_e/d\rho \propto 1/\chi_e$, the $\Delta T_e \propto \Delta\rho/\bar{\chi}_e$ between rational surfaces is dominated by radii where χ_e^{flutt} is smallest and thermal insulation is maximized. Dots indicate radially-averaged electron thermal diffusivities $\bar{\chi}_e$ between successive rational surfaces. The top red dashed lines and dots show possible thin magnetic island effects (as approximated in [15]) at the rational surfaces. While the estimated island effects are too large, the effective flutter $\bar{\chi}_e$ prediction agrees with the experimental results reasonably well. Its thermal diffusivity hill flattens the T_e gradient at the pedestal top and thus can stabilize P-B modes.

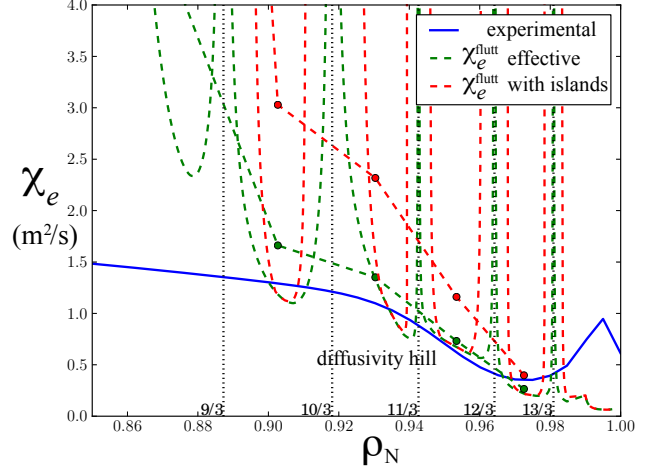


Fig. 4 Electron thermal diffusivities in the pedestal region of DIII-D #126006 in which RMPs are used to suppress ELMs: experimental (blue, solid line), effective ambipolar-constrained (green, dashed) and with thin islands at rational surfaces (red, top dashed). Dots show radially averaged $\bar{\chi}_e$'s [15]. Adapted from Ref. [16].

Previous flutter validation studies [16] have used the ambipolar constraint $\Gamma_e^{\text{flutt}} = 0$. However, in general the radial electric field required for ambipolar density transport should be determined by equating the non-ambipolar electron (3D, RMP-flutter-induced) and ion (2D, symmetric) pedestal density fluxes, which can be written as [15]

$$\Gamma_e^{\text{flutt}}(E_\rho) = -n_e D_e (e/T_e) (E_\rho - E_\rho^{\text{flutt}}), \quad \Gamma_i^{\text{sym}}(E_\rho) = n_i D_i^{\text{sym}} (Z_i e/T_i) (E_\rho - E_\rho^{\text{sym}}). \quad (9)$$

When RMPs are applied, the quasineutrality (ambipolar flow) condition $\Gamma_i^{\text{sym}}(E_\rho^{\text{sym}}) = \Gamma_e^{\text{flutt}}(E_\rho^{\text{sym}})$ yields

$$E_\rho^{\text{amb}} = \frac{E_\rho^{\text{sym}} + \kappa E_\rho^{\text{flutt}}}{1 + \kappa}, \quad \kappa \equiv \frac{T_i}{T_e} \frac{D_e}{D_i^{\text{sym}}} = \frac{E_\rho^{\text{amb}} - E_\rho^{\text{sym}}}{E_\rho^{\text{flutt}} - E_\rho^{\text{amb}}} \propto \delta \hat{B}_\rho^2. \quad (10)$$

Here, κ represents the relative strength of the non-ambipolar flutter-induced electron diffusivity compared to that of the ions. This parameter is the inverse of an analogous parameter postulated in Eq. (13) in Ref. [40]. The net RMP-flutter-induced electron ambipolar density and heat fluxes evaluated at E_ρ^{amb} are specified in Ref. [15].

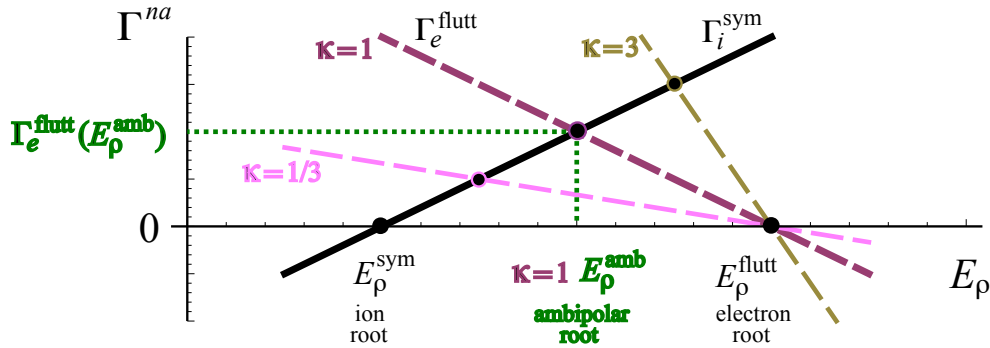


Fig. 5 Dependence of electron and ion non-ambipolar density fluxes on the radial electric field. The sensitivity of the electron flux to E_ρ increases with the strength of the RMPs, which is indicated here by different values of the parameter $\kappa \propto \delta \hat{B}_\rho^2$. The dotted lines indicate the electric field required for ambipolarity and the resultant ambipolar density flux for $\kappa = 1$. Copyright © 2013 by IOP Publishing and International Atomic Energy Agency [15].

5 Pedestal plasma transport equations

In low collisionality tokamak pedestals, FSAs of plasma equations are appropriate because the electron and ion collision lengths ($\lambda \gtrsim 300$ m) are longer than the toroidal circumference ($\gtrsim 10$ m). The FSA parallel (to \mathbf{B}_0) equilibrium ($t > 1/\nu_e \sim 10^{-5}$ s) electron force balance $0 = -n_e e \langle \mathbf{B}_0 \cdot \mathbf{E}^A \rangle - \langle \mathbf{B}_0 \cdot \nabla \cdot \boldsymbol{\pi}_{e\parallel} \rangle + n_e e \langle \mathbf{B}_0 \cdot \mathbf{J} \rangle / \sigma_{\parallel}^{\text{Sp}}$ yields the tokamak parallel Ohm's law [41]: $\langle \mathbf{B}_0 \cdot \mathbf{J}_0 \rangle = (1/\eta_{\parallel}^{\text{nc}}) \langle \mathbf{B}_0 \cdot \mathbf{E}^A \rangle + \langle \mathbf{B}_0 \cdot \mathbf{J}_{\text{bs}} \rangle$. Here, $\mathbf{E}^A = -\partial \mathbf{A} / \partial t \simeq -(\partial \Psi_p / \partial t) \nabla \zeta$ is the Ohmic electric field and $\langle \mathbf{B}_0 \cdot \nabla \cdot \boldsymbol{\pi}_{e\parallel} \rangle$ is the ‘‘neoclassical’’ parallel viscous force closure [24] induced by parallel stress in the electron fluid caused by collisions of flow-carrying untrapped electrons with trapped particles. The corresponding parallel ion viscous force closure $\langle \mathbf{B}_0 \cdot \nabla \cdot \boldsymbol{\pi}_{i\parallel} \rangle \sim \rho_m \mu_i \mathbf{V}_i \cdot \nabla \theta / \mathbf{B}_0 \cdot \nabla \theta$ damps the poloidal ion flow at a rate $\mu_i \lesssim \nu_i$ to an ion-temperature-gradient-driven value. Combined with the MHD-enforced radial ion force balance, for times longer than the ion collision time ($t > 1/\nu_i \sim 1$ ms) this yields

$$\Omega_t \equiv \langle \mathbf{V}_i \cdot \nabla \zeta \rangle = - \left(\frac{d\Phi_0}{d\psi_p} + \frac{1}{n_i q_i} \frac{dp_i}{d\psi_p} \right) + \frac{c_p}{q_i} \frac{dT_i}{d\psi_p} = \frac{E_\rho}{RB_p} - \Omega_{*i} + \Omega_p, \quad (11)$$

which relates the plasma toroidal rotation frequency Ω_t to the radial electric field E_ρ , but does not specify either.

In tokamaks the toroidal magnetic flux ψ_t is relatively constant in time since it is determined mainly by steady currents flowing in toroidal magnetic field coils; thus, $\partial \psi_t / \partial t|_{\mathbf{x}} \simeq 0$. In contrast, the poloidal magnetic flux ψ_p can change on the transport time scale relative to ψ_t [24, 41]: $\dot{\psi}_p \equiv \partial \psi_p / \partial t|_{\psi_t} = D_\eta \Delta^+ \psi_p - S_{\psi_p}$. Here, Δ^+ is a second order cylindrical-like differential operator in ρ and $S_{\psi_p} = \partial \Psi_p / \partial t + \eta_{\parallel}^{\text{nc}} \langle \mathbf{B}_0 \cdot \mathbf{J}_{\text{bs}} \rangle / (I \langle R^{-2} \rangle)$ represents the sources of poloidal magnetic flux produced by the Ohmic transformer and bootstrap current.

Collision-induced neoclassical plasma transport [28, 24] in tokamaks is calculated relative to poloidal magnetic flux surfaces — because to lowest order the canonical toroidal angular momentum $p_\zeta \equiv \mathbf{e}_\zeta \cdot (m_s \mathbf{v} + q_s \mathbf{A}) = m_s R^2 \mathbf{v} \cdot \nabla \zeta - q_s \psi_p$ ties particles to a particular ψ_p to lowest order in the gyroradius. Here, $\mathbf{e}_\zeta \equiv R^2 \nabla \zeta = R \hat{\mathbf{e}}_\zeta$ is the (covariant) toroidal angular base vector. Plasma microinstabilities and transport they induce are also calculated relative to ψ_p . Thus, to describe radial plasma transport in tokamaks, fluid moment equations for n_s , \mathbf{V}_s , p_s , are first transformed [24, 41, 42] from laboratory coordinates to poloidal magnetic flux coordinates. However, because the toroidal flux is nearly constant in time, $\rho \propto \sqrt{\psi_t}$ is used as the radial coordinate. Adding sources of density S_n , momentum \mathbf{S}_m and energy S_E and taking the FSA, the tokamak transport equations for the plasma density n and total toroidal angular momentum density $L_t \equiv \rho_m \langle R^2 \rangle \Omega_t$, and species pressures p_s are [42]

$$\text{density:} \quad \frac{1}{V'} \frac{\partial}{\partial t} \Big|_{\psi_p} \langle n \rangle V' + \dot{\rho}_{\psi_p} \frac{\partial \langle n \rangle}{\partial \rho} + \frac{1}{V'} \frac{\partial}{\partial \rho} (V' \Gamma) = \langle \bar{S}_n \rangle, \quad (12)$$

$$\text{tor. mom.:} \quad \frac{1}{V'} \frac{\partial}{\partial t} \Big|_{\psi_p} L_t V' + \dot{\rho}_{\psi_p} \frac{\partial L_t}{\partial \rho} + \frac{1}{V'} \frac{\partial}{\partial \rho} (V' \bar{\Pi}_{\rho\zeta}) = \langle \mathbf{e}_\zeta \cdot (\bar{\mathbf{J}} \times \bar{\mathbf{B}} - \nabla \cdot \bar{\boldsymbol{\Pi}} + \bar{\mathbf{S}}_m) \rangle, \quad (13)$$

$$\text{energy:} \quad \frac{3}{2} \langle p_s \rangle \frac{\partial}{\partial t} \Big|_{\psi_p} \ln \langle p_s \rangle V'^{5/3} + \frac{3}{2} \dot{\rho}_{\psi_p} \frac{\partial \langle p_s \rangle}{\partial \rho} + \frac{1}{V'} \frac{\partial}{\partial \rho} (V' \Upsilon_s) + \langle \nabla \cdot \mathbf{q}_{s*}^{\text{pc}} \rangle = \bar{Q}_{s \text{ net}}. \quad (14)$$

Here, $V' \langle n \rangle$ and $V' L_t$ are the number of plasma particles and plasma toroidal angular momentum between the ρ and $\rho + d\rho$ flux surfaces. Both are adiabatic (isentropic) plasma properties that are conserved in the absence of fluid closures and sources. Similarly, $\ln \langle p_s \rangle V'^{5/3}$ is the collisional entropy between the ρ and $\rho + d\rho$ flux surfaces, which is also a conserved quantity in the absence of closures and sources. Further, $\dot{\rho}_{\psi_p} \equiv -\dot{\psi}_p / \psi'_p$ in which $\psi'_p \equiv \partial \psi_p / \partial \rho = RB_p$ takes account of possible ψ_p surface motion relative to $\rho(\psi_t)$.

6 Summary

In the absence of RMPs, the paleoclassical predictions in (5) and (4) provide [10, 11, 12] the minimum electron temperature gradient and (via its intrinsic density pinch) maximum density in the pedestal steep gradient region (II, III). When RMPs are added, the magnetic flutter model [13, 14, 15] provides reasonable predictions for the RMP-induced increase in χ_e at the pedestal top [16] and procedures [15] for determining the increase in the radial electric field E_ρ [or via (11), alternatively $\Omega_t = L_t / (\rho_m \langle R^2 \rangle)$ from the solution of (13)] and the increase in ambipolar density transport it causes. While paleoclassical and flutter transport provide the underlying basis

for modeling H-mode pedestals, many other processes can add to their “irreducible minimum” levels of pedestal plasma transport. More generally, the radial electric field (or $L_t \equiv \rho_m \langle R^2 \rangle \Omega_t$ which determines Ω_t and hence E_p) needs to be considered in conjunction with solving for n , p_e and p_i in the pedestal on the transport time scale.

At the pedestal top (I), core transport transitions to anomalous transport due to MTM, ETG and ITG micro-turbulence. In the steep gradient region (II, III), KBMs may limit the achievable total pressure gradient, and additional ambipolar density transport and ion neoclassical thermal diffusivity can be important. In the pedestal bottom (III) 2D effects of ion orbit losses and neutral fueling become important [9] and RMPs cause small fractions of field lines to connect to divertor plates. Finally, FSA toroidal-flux-based modeling codes inside the separatrix need to be coupled to 2D and 3D poloidal-flux-based SOL and boundary codes outside the separatrix.

Acknowledgements The author is grateful to the program committee of the 14th International Workshop on “Plasma Edge Theory in Fusion Devices,” 23–25 September 2013, Cracow, Poland for inviting him to present this work at this PET-14 workshop. He is also grateful to his many colleagues in Refs. [9]–[16] and [41], [42] who have contributed to the work summarized in this paper. This research was supported by U.S. DoE grants DE-FG02-86ER53218 and DE-FG02-92ER54139.

References

- [1] R. Aymar, V.A. Chuyanov, M. Huguet, Y. Shimomura et al., Nucl. Fusion **41**, 1301 (2001); <http://iter.org>.
- [2] P.B. Snyder, H.R. Wilson, J.R. Ferron et al., Phys. Plasmas **9**, 2037 (2002).
- [3] R.J. Groebner et al., Nucl. Fusion **53**, 093024 (2013).
- [4] T.E. Evans et al., Nature Phys. **2**, 419 (2006).
- [5] T.E. Evans et al., Phys. Plasmas **13**, 056121 (2006).
- [6] W. Suttrop et al., Plasma Phys. Control. Fusion **53**, 124014 (2011).
- [7] A. Kirk et al., Nucl. Fusion **53**, 043007 (2012).
- [8] T.E. Evans et al., Nucl. Fusion **48**, 024002 (2008).
- [9] J.D. Callen, R.J. Groebner, T.H. Osborne, J.M. Canik, L.W. Owen, A.Y. Pankin, T. Rafiq, T.D. Rognlien and W.M. Stacey, Nucl. Fusion **50**, 064004 (2010).
- [10] J.D. Callen, J.M. Canik and S.P. Smith, Phys. Rev. Lett. **108**, 245003 (2012).
- [11] J.M. Canik et al., Phys. Plasmas **18**, 056118 (2011).
- [12] S.P. Smith, J.D. Callen, R.J. Groebner, T.H. Osborne, A.W. Leonard, D. Eldon, B.D. Bray and the DIII-D Team, Nucl. Fusion **52**, 114016 (2012).
- [13] J.D. Callen, A.J. Cole, C.C. Hegna, S. Mordijck, and R.A. Moyer, Nucl. Fusion **52**, 114005 (2012).
- [14] J.D. Callen, A.J. Cole, and C.C. Hegna, Phys. Plasmas **19**, 112505 (2012).
- [15] J.D. Callen, C.C. Hegna, and A.J. Cole, Nucl. Fusion **53**, 113015 (2013).
- [16] P.T. Raum, S.P. Smith, J.D. Callen, N. Ferraro, O. Meneghini, “Modeling of Magnetic Flutter Induced Transport in DIII-D,” report GA-A257559, July 2013 (submitted to Nuclear Fusion).
- [17] W.M. Stacey, Contrib. Plasma Phys. **48**, 94 (2008).
- [18] J.D. Callen, Phys. Plasmas **12**, 092512 (2005).
- [19] J.D. Callen et al., Nucl. Fusion **47**, 1449 (2007).
- [20] J.D. Callen, Phys. Plasmas **14**, 040701 (2007).
- [21] J.W. Connor, R.J. Hastie, and J.B. Taylor, Phys. Plasmas **15**, 014701 (2008).
- [22] J.D. Callen, Phys. Plasmas **15**, 014702 (2008).
- [23] J.D. Callen, “Model for pedestal structure,” Report UW-CPTC 11-4R, 7 November 2011 which is available as UW-CPTC 11-4.rev via <http://www.cptc.wisc.edu/Reports.html>.
- [24] S.P. Hirshman and D.J. Sigmar, Nucl. Fusion **21**, 1079 (1981).
- [25] C.T. Hsu, K.C. Shaing, R.P. Gormley and D.J. Sigmar, Phys. Fluids B **4**, 4023 (1992).
- [26] Y.B. Kim, P.H. Diamond and R.J. Groebner, Phys. Fluids B **3**, 2050 (1991); Erratum, Phys. Fluids B **4**, 2996 (1992).
- [27] See UW-CPTC 09-6R available as supplementary material for Reference [11] in Reference [42] below via <http://ftp.aip.org/epaps/phys Plasmas/E-PHPAEN-17-033091/033091php.pdf>.
- [28] F.L. Hinton and R.D. Hazeltine, Rev. Mod. Phys. **48**, 239 (1976).
- [29] O. Sauter, C. Angioni and Y.R. Lin-Liu, Phys. Plasmas **6**, 2834 (1999).
- [30] G.D. Garstka et al., Nucl. Fusion **46**, S603 (2006).
- [31] J.D. Callen, Nucl. Fusion **51**, 094026 (2011).
- [32] P.B. Snyder et al., Phys. Plasmas **19**, 056115 (2012).
- [33] M.R. Wade et al., paper EX/3-1 at 8–13 October 2012 San Diego IAEA Fusion Energy Conference; www-naweb.iaea.org/naweb/physics/FEC/FEC2012/html/fec12.htm.
- [34] M.F. Heyn et al., Nucl. Fusion **48**, 024005 (2008).
- [35] Liu Y., Kirk A. and Nardon E., Phys. Plasmas **17**, 122502 (2010).
- [36] M.S. Chu et al., Nucl. Fusion **51**, 073036 (2011).
- [37] M. Becoulet et al., Nucl. Fusion **52**, 054003 (2012).
- [38] N.M. Ferraro, Phys. Plasmas **19**, 056105 (2012).
- [39] N.M. Ferraro et al., Nucl. Fusion **53**, 073042 (2013).
- [40] E. Kaveeva, V. Rozhansky and M. Tendler, Nucl. Fusion **48**, 075003 (2008).
- [41] J.D. Callen, A.J. Cole, and C.C. Hegna, Phys. Plasmas **16**, 082504 (2009).; Erratum, Phys. Plasmas **20**, 069901 (2013).
- [42] J.D. Callen, C.C. Hegna, and A.J. Cole, Phys. Plasmas **17**, 056113 (2010).